Inorganic Chemistry

Article

Superconducting YAu₃Si and Antiferromagnetic GdAu₃Si with an Interpenetrating Framework Structure Built from 16-Atom Polyhedra

Girma Hailu Gebresenbut,* Lars Eriksson, Ulrich Häussermann, Andreas Rydh, Roland Mathieu, Olga Yu. Vekilova, and Takayuki Shiino*

Read Online

ACCESS | Metrics & More | Article Recommendations | Supporting Information

ABSTRACT: Investigations of reaction mixtures $RE_x(Au_{0.79}Si_{0.21})_{100-x}$ (RE = Y and Gd) yielded the compounds REAu₃Si which adopt a new structure type, referred to as GdAu₃Si structure ($tP80$, $P4_2/mnm$, $Z = 16$, $a = 12.8244(6)/12.7702(2)$ Å, and $c = 9.0883(8)/9.0456(2)$ Å for GdAu₃Si/YAu₃Si, respectively). REAu₃Si was afforded as millimeter-sized faceted crystal specimens from solution growth employing melts with composition $RE_{18}(Au_{0.79}Si_{0.21})_{82}$. In the GdAu₃Si structure, the Au and Si atoms are strictly ordered and form a framework built of corner-connected, Si-centered, trigonal prismatic units $SiAu_6$. RE atoms distribute on 3 crystallographically different sites and each attain a 16-atom coordination by 12 Au and 4 Si atoms. These 16-atom polyhedra commonly fill the space of the unit cell. The physical properties of REAu₃Si were investigated by heat capacity, electrical resistivity, and magnetometry techniques and are discussed in the light of theoretical predictions. YAu₃Si exhibits superconductivity around 1 K, whereas GdAu₃Si shows a complex magnetic ordering, likely related to frustrated antiferromagnets exhibiting chiral spin textures. GdAu₃Si-type phases with interesting magnetic and transport properties may exist in an extended range of ternary RE−Au−Si systems, similar to the compositionally adjacent cubic 1/1 approximants $RE(Au,Si)_{\sim 6}$.
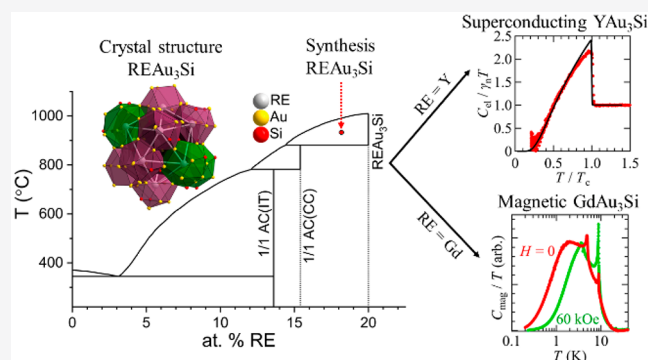
1. INTRODUCTION

Polar intermetallic compounds of gold with electropositive and post-transition metals/semimetals from groups 12−14 display peculiarities in their structural chemistry and physical properties, which has been attributed to the extraordinarily high electronegativity of gold (which is the highest among metallic elements) and associated relativistic effects in chemical bonding.[1] The family of gold polar intermetallics is rather diverse and also includes icosahedral quasicrystals (iQCs), such as i-Na−Au−Ga, i-Ca−Au−Al(Ga)(In), i-RE−Au−Al (RE = Yb and Tm), i-RE−Au−Sn (RE = Ca and Yb), and a larger range of 1/1 cubic approximant crystal (AC) phases.[2−11]

The majority of gold-based iQCs are of Tsai-type[12] and also contain rare-earth (RE) elements. These iQCs have attracted considerable attention because of expectations about unique physical properties associated to the quasiperiodic structure.[13,14] Tsai-type iQCs are distinguished by their atomic cluster building unit ("Tsai-cluster") consisting of four concentric shells and centered by a tetrahedral moiety.[15] The radial dimension of a Tsai-cluster in gold-based iQCs is 15−16 Å. Their related 1/1 ACs are also built from Tsai-clusters and have similar chemical composition but are conventional (3D periodic) crystals.[16] In both Tsai-type QCs and 1/1 ACs, RE

atoms are arranged into icosahedra which represent one of the shells of a Tsai-cluster. AC phases play a pivotal role by providing local structural information (from standard crystallographic techniques) needed to determine the structures of iQCs and by providing references for physical properties of 3D periodic systems. Since the stability of Tsai-type QCs is linked to a very narrow valence electron per atom ratio, 1/1 ACs are found much more frequently than QCs.[17] There are many phase diagrams (i.e., RE−Au−Si and RE−Au−Ge) for which hitherto only the 1/1 AC phase is known.

We recently reported that for Tsai-type 1/1 ACs in RE−Au−Si systems (RE; e.g., Gd, Tb, and Ho) the central tetrahedron of the Tsai clusters can be systematically replaced by a single RE atom, giving rise to a distinctly different variant of 1/1 AC phase with a composition $RE_{\sim 15.4}(Au,Si)_{\sim 84.6}$
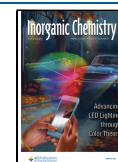
instead of $RE_{\sim13.6}(Au,Si)_{\sim86.4}$.[18] The regular ((Au,Si) tetrahedron centered) and RE-centered phase were termed AC(IT) and AC(CC), respectively. During the course of this study we discovered an even more RE-rich phase, which formed from the peritectic decomposition of AC(CC) at temperatures above 900 °C. In this paper, we report on the strictly Au,Si ordered structure and the physical properties of $REAu_3Si$ (RE = Y and Gd). With an RE content of 20 at. % the structure of $REAu_3Si$ significantly deviates from the Tsai-type cluster based and Au,Si disordered 1/1 AC structure, yet locally similarities are maintained (i.e., a 16-atom coordination environment for RE and icosahedral arrangement of RE atoms).

2. METHODS

2.1. Synthesis. The starting materials were granules of the elements Gd and Au (Chempur 99.99%), Y (Chempur 99.9%), and Si (Highways International 99.999%). Prior the synthesis reactions, Au and Si were arc-melted in a ratio 79:21 (at. %) corresponding to the eutectic composition in the Au−Si phase diagram. The arc-melting procedure was repeated five-times to get homogeneous ingot. Actual reaction mixtures then constituted compositions $Gd_x(Au_{0.79}Si_{0.21})_{100-x}$ with x in the range of 15−18. Reaction mixtures were investigated with differential scanning calorimetry (DSC) prior to solution-growth synthesis to extract liquid temperatures. Synthesis reactions targeting $REAu_3Si$ were carried out in alumina (Al_2O_3) crucibles from LSP Industrial Ceramics (USA), in the form of "Canfield Crucible Sets (CCS)". The CCS consists of two flat-bottomed cylindrical crucibles and an alumina frit-disc with holes of $\sim0.7-1$ mm in diameter designed to separate solid grains from the liquid melt during centrifugation.[19] A total mass of about 3 g was weighed inside a glovebox (Ar-atmosphere, <0.1 ppm O_2) and loaded into the CCS, which was then encapsulated inside a stainless-steel ampule. Ampules were heated in a commercial multistep programmable muffle furnace to 1050 °C over a period of 10 h and dwelled for 3 h to ensure a homogeneous melt. Subsequently, the temperature was lowered to 920 °C using a cooling rate of 1 °C/h, and reactions were terminated by isothermally centrifuging off excess melt at the target temperatures.

2.2. Phase and Structure Analysis. The samples were studied with powder X-ray diffraction (PXRD), single-crystal X-ray diffraction (SCXRD), DSC, scanning electron microscopy (SEM) coupled with energy-dispersive X-ray spectroscopy (EDX), and magnetic property measurements. A Bruker D8 powder diffractometer with $\theta-2\theta$ diffraction geometry and a Cu $K\alpha$ radiation ($K\alpha_1$ = 1.540598 Å and $K\alpha_2$ = 1.544390 Å) was used for collecting PXRD intensities at room temperature. PXRD data were analyzed with the HighScore Plus 3.0 software from PANalytical[20] and the Fullprof Suite.[21] Powdered samples were applied to a zero-diffraction plate, and diffraction patterns were measured in a 2θ range of 7−90°. A Bruker D8 VENTURE single-crystal X-ray diffractometer with Mo $K\alpha$ radiation ($K\alpha$ = 0.71073 Å) with Incoatec microfocus source (IμS 3.0) and Photon II CCD area detector was utilized to collect SCXRD intensities at room temperature. Diffraction data covering a half (full) sphere in reciprocal space were collected with 100% completeness. SCXRD data reduction and numerical absorption corrections were carried out using the APEX III software from Bruker.[22] The crystal structure was solved and refined using the software SHELXT[23] and JANA2006,[24] respectively. The structures were visualized using Diamond 3.2K4.[25] Electron densities were visualized using the software VESTA.[26] DSC measurements were carried out with a NETZSCH STA 449 F1 Jupiter instrument. Sample specimens (typically faceted grains, $REAu_3Si$) with total mass of ~50 mg were placed in polycrystalline sapphire crucibles (OD = 5 mm, ID = 4 mm) and a heating/cooling cycle to 1150 °C was carried out at a rate of 10 °C/minute under an Ar flow of ~40 mL/min. An empty crucible served as reference. The crucibles used for the actual DSC measurement were first carried through identical heating/cooling protocol to the sample and the data were used as background. Scanning electron microscopy (SEM) investigations employed a

Zeiss−Merlin instrument equipped with energy-dispersive X-ray (EDX) spectroscopy for elemental analysis with X-Max 80 mm^2 Silicon Drift Detector with high sensitivity and high count rates. Prior to the SEM/EDX experiments samples were cross section polished gently for 20 h using Ar$^+$-ion beam in a Cross-Section Polisher SM-09011 instrument from JEOL. EDX data was collected with an acceleration voltage of 20 kV over larger areas ($\sim100 \times 100~\mu m^2$) on at least 20 points.

2.3. Physical Property Measurements. (Polycrystalline) samples for physical property measurements were prepared from pieces of crushed specimens obtained from the solution-growth synthesis experiments. Direct current (dc) magnetization measurements (on ~10 mg sample specimens) were carried out using an MPMS XL SQUID magnetometer equipped with a superconducting magnet (up to ±50 kOe) and a Physical Property Measurement System (PPMS) with a superconducting magnet (up to ±90 kOe), both from Quantum Design, Inc. Heat capacity measurements were carried out using a Bluefors dilution refrigerator equipped with a superconducting magnet (up to ±120 kOe). The heat capacity data was collected down to 100−200 mK on tiny sample fragments (with a volume of approximately $1 \times 10^5~\mu m^3$) using a differential membrane-based nanocalorimeter.[27] We calibrated the specific-heat values in molar unit by multiplying the heat capacity data by a constant to match the model curve of $\gamma T + C_D$ at high temperatures, where γ is the electronic specific heat coefficient (we determined $\gamma = 1$ mJ/K^2 mol for GdAu$_3$Si and YAu$_3$Si) and C_D is the specific heat of the Debye model (we determined the Debye temperature θ_D = 170 K for GdAu$_3$Si and θ_D = 193 K for YAu$_3$Si); see also ref 28. The electrical resistivity (for sample specimens with dimension $\sim0.2 \times 0.25 \times 1$ mm^3) was measured using the conventional four-probe method with the dilution refrigerator and the PPMS.

2.4. Theoretical Calculations. The ground state of GdAu$_3$Si was studied theoretically using a first-principles density functional theory (DFT) approach within the projector-augmented wave (PAW) method[29] as implemented in Vienna Ab Initio Simulation Package (VASP).[30−32] The generalized gradient approximation in its Perdew-Burke-Erzernhof flavor for exchange and correlation potential and energy was used.[33] All simulations of magnetic properties were done using the Molecular Dynamics Monte Carlo (MDMC) method.[34]

Standard approach at 0 K is to compare known magnetic orderings (for example, FM and simple AFM) and choose the state with the lowest total energy. In the case of complex magnetism, like different ferrimagnetic states, such an approach easily misleads to a wrong ground-state magnetic structure. The MDMC method[34] solves this issue. It finds the proper magnetic ordering in the course of standard first-principles calculations. At 0 K, the method is based on a Monte Carlo (MC) technique and efficiently explores the whole phase space of magnetic structures. At higher temperatures, the method takes care of coupling between spins and atomic vibrations via AIMD, and in particular can treat non-Heisenberg systems. Only collinear 0 K MDMC simulations were carried out in this work. Further, the obtained magnetic structures were tested by the noncollinear version of VASP and found to be collinear. All calculations referred to the 80 atom unit cell of magnetic GdAu$_3$Si. The structures were relaxed to p = 0 GPa with the accuracy of few kbar. A $2 \times 2 \times 2$ k-point Monkhorst−Pack grid[35] was used for all integrations over the Brillouin zone. LDA+U approximation in Dudarev's formulation[36] with $U = 6$ eV was applied on the f-electron states of Gd.[37] All the calculations were done at temperature $T = 0$ K. The energy cutoff for plane waves was set to 400 eV.

3. RESULTS AND DISCUSSION

3.1. Partial Pseudobinary RE−(Au$_{0.79}$Si$_{0.21}$) Systems and the Phase REAu$_3$Si. The deep eutectic point in the Au−Si phase diagram for Au$_{0.79}$Si$_{0.21}$ (~364 °C) has been previously exploited for the investigation of the (Au−Si)-rich part of ternary RE−Au−Si systems, considering these systems as pseudobinary RE$_x$(Au$_{0.79}$Si$_{0.21}$)$_{100-x}$ for x up to 15.[18,28] In these investigations melts with $x = 4-14$ were slowly cooled

over the liquidus which allows crystallization of the phases most rich in (Au−Si) below their peritectic decomposition temperatures (Figure 1). The solution growth experiments
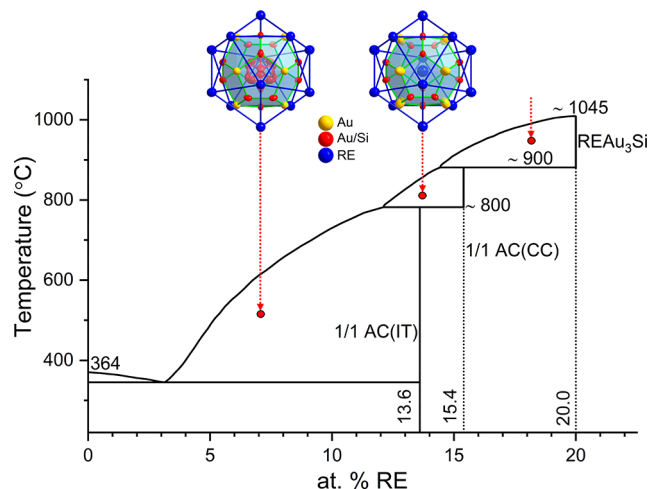
Figure 1. Sketch of the pseudobinary RE−$(Au_{0.79}Si_{0.21})$ partial phase diagram. The inset shows the two innermost shells of the Tsai cluster ((Au,Si) dodecahedron and RE icosahedron) which are centered with an orientationally disordered (Au,Si) tetrahedron (for AC(IT), left) and a single RE atom (for AC(CC), right), respectively; the red arrows indicate typical synthesis paths which were followed to prepare 1/1 AC(IT), 1/1 AC(CC), and REAu$_3$Si phases.

were terminated by centrifuging off isothermally excess liquid. High-melt crystallization typically affords ultrapure, single-crystalline products.[38] For x up to 10−11 they corresponded to regular 1/1 AC phase with an orientationally disordered $(Au,Si)_4$ tetrahedron at the Tsai-cluster center ((AC(IT)) cf. inset in Figure 1). For higher x (12−13), a variant of the 1/1 AC phase with a single RE atom at the cluster center was found (AC(CC)).[18,28] In this case, centrifugation temperatures above 800 °C had to be employed, and it is not (yet) clear whether the AC(CC)-phases are thermodynamically stable at low temperatures or represent high-temperature phases. The RE content in the AC(CC) phases is significantly increased (which has profound consequences to their magnetic properties[18]). However, the Au/Si composition of the AC(IT) and AC(CC) phases, $RE_{13.6}(Au_{\sim0.82}Si_{\sim0.18})_{86.4}$ and $RE_{15.4}(Au_{\sim0.81}Si_{\sim19})_{84.6}$, respectively, are very close to nominally employed $Au_{0.79}Si_{0.21}$ which justifies the pseudobinary approach.

AC(CC) phases undergo peritectic decomposition at around 900 °C into melt and a phase even more rich in RE.[18,28] This observation stimulated the extension of solution-growth experiments to the more RE-rich side for which melts with $x \approx 18$ and centrifugation temperatures around 920 °C were employed. For this study, RE = Y and Gd were chosen. As typical of this method, large (millmeter-sized) and facetted crystal specimens could be isolated (inset in Figure 2). EDX analyses of the synthesis products resulted in $Gd_{21.1(2)}Au_{60.9(2)}Si_{18.0(1)}$ and $Y_{19.7(1)}Au_{62.5(1)}Si_{17.8(1)}$; see Figure S1. This pointed strongly to a stoichiometric composition REAu$_3$Si and indicates that with increasing RE content ($x >$ 17−18) the phase diagram cannot be considered anymore as pseudobinary $RE_x(Au_{0.79}Si_{0.21})_{100-x}$. Figure 2 shows the PXRD patterns for GdAu$_3$Si and YAu$_3$Si. These are very similar and can be indexed to a primitive tetragonal lattice with $a \approx 12.8$ Å
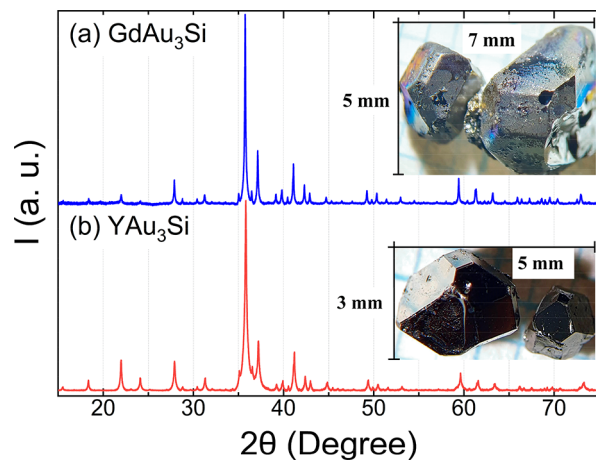
Figure 2. PXRD patterns for (a) GdAu$_3$Si and (b) YAu$_3$Si. X-ray scattering background and diffraction peaks from Cu $K\alpha_2$ radiation have been removed from each pattern for clarity. The inset photograph shows isolated grains from each sample.

and $c \approx 9.05$ Å. The whole diffraction profile fitting of the patterns, using the structure model obtained from SCXRD refinement, is shown in Figure S2.

Figure 3 shows the DSC traces for GdAu$_3$Si and YAu$_3$Si upon a heating and cooling cycle. The small event at 870/850
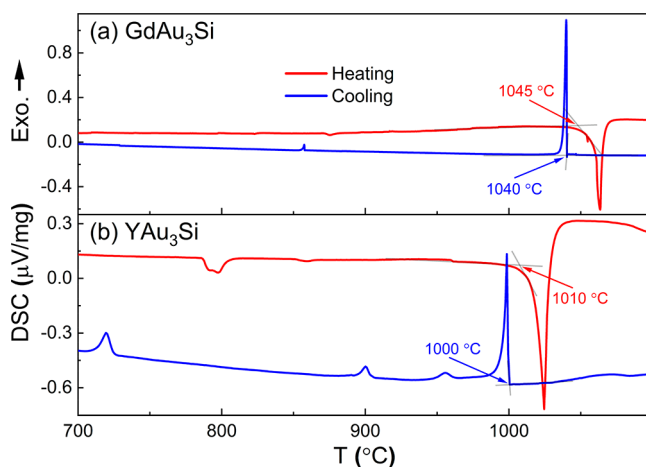
Figure 3. DSC traces for (a) GdAu$_3$Si and (b) YAu$_3$Si crystalline specimens. Temperatures of endothermic (decomposition) and exothermic (crystallization) events are estimated by extrapolation.

°C (heating/cooling) for GdAu$_3$Si is attributed to melting/crystallization of a small amount of residual flux with the composition $Au_{\sim0.9}Si_{\sim0.1}$ on the surface of the employed crystal specimen. The event at 1045/1040 °C indicates the liquid/solid temperature for the composition $Gd_{20}Au_{60}Si_{20}$ and most likely corresponds to congruent melting/solidification of GdAu$_3$Si, since the sample specimen after the DSC cycle appeared spherical and the PXRD pattern was virtually unchanged. In contrast, the heating trace of YAu$_3$Si shows several smaller but distinguished endothermic events before the pronounced event indicating formation of liquid phase (at around 1000 °C). An annealing experiment at 875 °C (after the first endothermic event) produced a mixture of YAu$_3$Si and AC(CC) phase (see Figures S3). Thus, the thermal behavior of YAu$_3$Si remains unclear. It may be suspected that this compound represents a (metastable) high-temperature phase

and that the exothermic conversion into the thermodynamic ground state at temperatures below 700 °C cannot be detected in DSC experiments because of a slow kinetics.

3.2. Crystal Structure of GdAu₃Si and YAu₃Si. The crystal structure of REAu₃Si was determined from single-crystal X-ray diffraction data. Refinement results are shown in Table 1

Table 1. SCXRD Refinement and EDX Results for REAu₃Si (RE = Gd and Y)

parameters	GdAu₃Si	YAu₃Si
empirical formula	GdAu₃Si	YAu₃Si
refined composition (at. %)	Gd₂₀Au₆₀Si₂₀	Y₂₀Au₆₀Si₂₀
EDX (at. %)	Gd₂₁.₁₍₂₎Au₆₀.₉₍₂₎Si₁₈.₀₍₁₎	Y₁₉.₇₍₁₎Au₆₂.₅₍₁₎Si₁₇.₈₍₁₎
formula weight	1552.5	1415.8
temperature/K	293	293
crystal system	tetragonal	tetragonal
space group	$P4_2/mnm$	$P4_2/mnm$
a/Å	12.8244(6)	12.7702(2)
c/Å	9.0883(8)	9.0456(2)
volume/Å³	1494.7(2)	1475.14(5)
Z	16	16
ρ_{calc}, g/cm³	13.7971	12.7492
μ/mm⁻¹	134.993	134.615
$F(000)$	5040.0	4640.0
radiation	Mo Kα (λ = 0.71073)	Mo Kα (λ = 0.71073)
2θ range, data collection/deg	4.5−63.04	4.52−83.88
index ranges	$-18 \leq h \leq 18$, $-18 \leq k \leq 18$, $-11 \leq l \leq 13$	$-24 \leq h \leq 23$, $-23 \leq k \leq 23$, $-16 \leq l \leq 16$
reflections collected	15394	92034
ind. reflections [all data]	1349	2792[a]
ind. reflections [$I \geq 3\sigma(I)$]	1283	2283[a]
merging R indices	$R_{int} = 0.0267$, $R_{sigma} = 0.0266$	$R_{int} = 0.0572$, $R_{sigma} = 0.0510$
constraint/ restraint/ parameter	0/0/114	19/0/174[a]
goodness-of-fit [all data]	2.12[b]	1.73[b]
goodness-of-fit [$I \geq 3\sigma(I)$]	2.13[b]	1.82[b]
final R indexes [$I \geq 3\sigma(I)$]	$R_1 = 0.0183$, $wR_2 = 0.0469$	$R_1 = 0.0249$, $wR_2 = 0.0471$
final R indexes [all data]	$R_1 = 0.0204$, $wR_2 = 0.0479$	$R_1 = 0.0373$, $wR_2 = 0.0497$
largest diff. peak/ hole/e Å⁻³	3.89/−1.62	4.63/−3.59

[a]Due to structural (positional) disorder in YAu₃Si, the data collection strategy was extended to cover a full-sphere in reciprocal space with narrow step widths and longer exposure times; more parameters were refined. [b]The relatively higher GOF values come partly from using the program Jana2006.

and independent atomic positions and displacement parameters are listed in Table 2. The primitive tetragonal unit cell (space group $P4_2/mnm$ (#136)) contains 80 atoms which are distributed over 9 crystallographically independent sites: 5 Au, 3 Gd, and 1 Si. There is no detectable chemical (Au/Si) disorder, which is characteristic for the 1/1 AC systems. However, unlike in the GdAu₃Si compound, an $8i$ Au position was found positionally disordered in YAu₃Si (see Figure S4).

Hence, the position was modeled as a mutually exclusive Au3/ Au3′ split position with ~0.93/0.07 occupancies, respectively. Furthermore, the atomic displacement parameters for YAu₃Si are about twice that for GdAu₃Si. This and the positional disorder may also be indicating a room temperature metastable nature of YAu₃Si. The following description of the structure will be based on the parameters for GdAu₃Si. Table 3 lists relevant interatomic distances (an extended distance table is given in Table S1).

The GdAu₃Si structure may be described using the Gd coordination polyhedra which possess the local symmetries $4e$ ($2mm$), $4f$ ($m2m$), and $8i$ (m), as shown in Figure 4a. Each Gd atom is surrounded by 12 Au and 4 Si atoms, which provide a well-defined coordination shell with Gd−(Au,Si) distances in a range of 3.03−3.47 Å (cf. Table 3), clearly separated from next-nearest-neighbor distances starting off at 4.43 Å. The three kinds of polyhedra commonly provide space filling (Figure 4b). Their linkage can also be visualized as interpenetrating network (Figure 4c): Gd1 polyhedra are condensed into rows along the [001] direction via shared rectangular faces. These rows are linked by Gd2 polyhedra in the [110] direction to yield a primitive cubic arrangement with channels along (1/2, 0, z), which is the direction of the 4_2 axes. This network is interpenetrated by the framework formed by Gd3 polyhedra. Gd3 polyhedra are clustered into rows (via the 4_2 operations) along the c-direction and rows are connected via rectangular faces in the [110] direction. Si atoms are strictly coordinated by 6 Au atoms in a trigonal prismatic fashion (Si− Au distances are in a narrow range 2.45−2.59 Å, cf. Table 3), and the Au₃Si partial structure corresponds to an array of corner connected SiAu₆/₂ trigonal prisms (Figure 4d). Considering REAu₃Si as polar intermetallics, the Au₃Si substructure bears a polyanionic character. In this picture, bonding between Au−Au and Au−Si atoms is of a strong covalent nature, whereas interactions between RE (RE³⁺) and Au/Si are essentially electrostatic. In the electronic density of states (DOS) of REAu₃Si states near the Fermi level originate from Au−d states with minor contributions from Si and Gd orbitals (cf. Figure S5). This resembles strongly to other gold-rich polar intermetallics, such as RE₃Au₇Sn₃, for which a pronounced polar intermetallic character has been proven from detailed bonding analyses.[39]

Yet a different view of the GdAu₃Si structure is provided when analyzing the Gd partial structure and identifying Gd2 atoms at the center of icosahedra formed by 4 Gd1 and 8 Gd3 atoms (Figure 5a). Gd2−Gd distances are in a range of 4.73− 5.42 Å, and the edge lengths are between 3.94 and 5.42 Å (cf. Table 3). These icosahedral clusters in turn are arranged in a bcc-like (8 + 6) fashion (Figure 5b), where the nearest-neighbor centers (8) are 7.9 Å apart and the distance to the next-nearest-neighbor centers is on average 9.1 Å (Figure 5c). The icosahedral arrangement of Gd reminds of to the 1/1 AC structure, albeit icosahedra in the tetragonal GdAu₃Si structure are more distorted and in addition appear more compressed (the center to corner distances of 1/1 AC icosahedra are in a range of 5.2−5.71 Å).[18] Similar to the cubic 1/1 AC structure, the tetragonal GdAu₃Si structure may represent a robust structure type that is realized for a larger number of REAu₃Si and REAu₃Ge compounds and thus could provide a playground for studying various physical properties and property changes when varying RE. In the following, we show superconductivity for YAu₃Si and a peculiar magnetic behavior for GdAu₃Si.

Table 2. Atomic Coordinates and Equivalent Atomic Displacement Parameters (U_{eq}) of Independent Atomic Positions for REAu$_3$Si (RE = Gd and Y) Obtained from SCXRD Refinement[a]

atom	Wyck.	S.O.F.	x/a	y/b	z/c	$U_{eq.}$ [Å^2]
			GdAu$_3$Si			
Gd1	4e	1	1/2	1/2	0.2169(2)	0.0105(2)
Gd2	4f	1	0.22224(8)	0.22224(8)	0	0.0163(3)
Gd3	8i	1	0.63183(8)	0.11657(8)	0	0.0109(2)
Au1	8i	1	0.46064(6)	0.30558(7)	0	0.0130(2)
Au2	8j	1	0.32172(4)	0.32172(4)	0.7248(1)	0.0142(1)
Au3	8i	1	0.49648(7)	0.34779(6)	1/2	0.0162(2)
Au4	8j	1	0.66983(5)	0.33017(5)	0.8422(1)	0.0153(1)
Au5	16k	1	0.41023(5)	0.10204(5)	0.84455(6)	0.0163(1)
Si1	16k	1	0.5118(3)	0.2552(3)	0.7334(5)	0.0150(9)
			YAu$_3$Si			
Y1	4e	1	1/2	1/2	0.2168(3)	0.0253(9)
Y2	4f	1	0.2228(1)	0.2228(1)	0	0.0283(4)
Y3	8i	1	0.6317(1)	0.1166(1)	0	0.0208(3)
Au1	8i	1	0.46101(5)	0.30589(5)	0	0.0276(4)
Au2	8j	1	0.66978(4)	0.33022(4)	0.84199(9)	0.0322(4)
Au3	8i	0.933(5)	0.4985(2)	0.3464(2)	1/2	0.0331(9)
Au3′	8i	0.067(5)	0.474(1)	0.369(1)	1/2	0.0331(9)
Au4	8j	1	0.82152(4)	0.17848(4)	0.77523(9)	0.0293(4)
Au5	16k	1	0.41031(4)	0.10177(4)	0.84458(6)	0.0323(4)
Si1	16k	1	0.5114(2)	0.2546(2)	0.7346(3)	0.0241(6)

[a]Wyckhoff positions (Wyck.) and site occupancy factors (S.O.F.) are listed. $U_{eq.} = 1/3(U_{11} + U_{22} + U_{33})$.

Table 3. Relevant Interatomic Distances in the GdAu$_3$Si Structure as Obtained from SCXRD Refinement

| atom pair		d/Å (<3.5 Å)	atom pair		d/Å (<6 Å)
	Au4	2x	3.1266(7)		Gd1	1x	3.942(2)
	Si1	4x	3.175(4)		Gd2	2x	4.782(1)
Gd1	Au1	4x	3.218(1)		Gd1	1x	5.146(2)
	Au3	4x	3.230(1)	Gd1	Gd2	2x	5.409(1)
	Au2	2x	3.2765(6)		Gd3	4x	5.561(1)
	Au3	2x	3.031(1)		Gd3	4x	5.581(1)
	Au2	2x	3.084(1)		Gd3	2x	4.731(2)
	Au5	4x	3.191(1)	Gd2	Gd3	4x	5.1251(8)
Gd2	Au1	2x	3.239(1)		Gd3	2x	5.425(2)
	Au4	2x	3.252(1)		Gd3	1x	4.514(2)
	Si1	4x	3.445(4)	Gd3	Gd3	1x	4.563(2)
	Si1	2x	3.117(4)		Gd3	4x	5.5530(9)
	Au3	1x	3.126(1)				
	Au4	2x	3.130(1)				
	Au5	2x	3.1733(6)				
Gd3	Au5	2x	3.179(1)				
	Au5	2x	3.185(1)				
	Au1	1x	3.270(1)				
	Au2	2x	3.276(1)				
	Si1	2x	3.377(4)				
	Au4	1x	2.452(2)				
	Au3	1x	2.476(2)				
	Au5	1x	2.509(2)				
Si1	Au5	1x	2.530(2)				
	Au1	1x	2.567(2)				
	Au2	1x	2.588(2)				

3.3. Superconducting YAu$_3$Si. Figure 6a shows the temperature dependence of the electrical resistivity for YAu$_3$Si. We observe a superconducting behavior at T_c = 0.94 K. The double-step behavior is attributed to a minor impurity of AC(CC) phase included in the YAu$_3$Si grain which was used

for this measurement. The Y–Au–Si AC(CC) phase has a slightly higher T_c.[28] The presence of tiny amounts of an AC(CC) impurity phase was also found for GdAu$_3$Si, and the reason for this is not clear since solution grown sample specimens are typically single phase. The impurity phase cannot be detected in PXRD and SEM analyses or specific heat measurements. It expresses only in the resistivity and low-field magnetization data.

Figure 6b shows the normalized electronic specific heat divided by temperature ($C_{el}/\gamma_n T$) as a function of normalized temperature (T/T_c), where C_{el} indicates the electronic contribution to the specific heat, and γ_n = 1.1 mJ/K^2 mol is the electronic specific heat coefficient in the normal state. Note that we subtracted the phonon contribution (estimated from the C/T vs T^2 plot) from the specific heat to estimate C_{el}. This confirms the bulk nature of the superconductivity. The overall behavior is similar to the weak-coupling Bardeen–Cooper–Schrieffer (BCS) model, suggesting that the superconductivity of YAu$_3$Si is of a conventional BCS type. We plot the upper critical field (H_{c2}) versus temperature in the inset of Figure 6b. From the lowest temperature value of H_{c2}, we estimate $H_{c2}(0)$ ≈ 3.9 kOe. From the data near T_c, we obtain dH_{c2}/dT = −4.86 kOe/K (cf. the solid line in the inset of Figure 6b), which allows us to estimate the orbital critical field at zero temperature using the Werthamer–Helfand–Hohenberg formula (in the dirty limit):[40] $H_{c2}^{orb}(0) = -0.693 T_c(\mathrm{d}H_{c2}/\mathrm{d}T) \approx$ 3.15 kOe. The $H_{c2}^{orb}(0)$ value is close to $H_{c2}(0)$; thus, the orbital effect mainly contributes to H_{c2} (rather than the spin paramagnetic effect).[40] The estimated values of superconducting parameters are listed in Table 4. From the specific heat, we estimate the thermodynamic critical field H_c by calculating the condensation energy. The Ginzburg–Landau (GL) parameter κ at $T = 0$ is then estimated from the relation $H_{c2} = \sqrt{2}\kappa H_c$.[41,42] Since $\kappa \gg 1/\sqrt{2}$, the superconductivity must be of type-II. See the caption of Table 4 for the other parameters. The overall superconducting behavior is similar to the Y–Au–Si
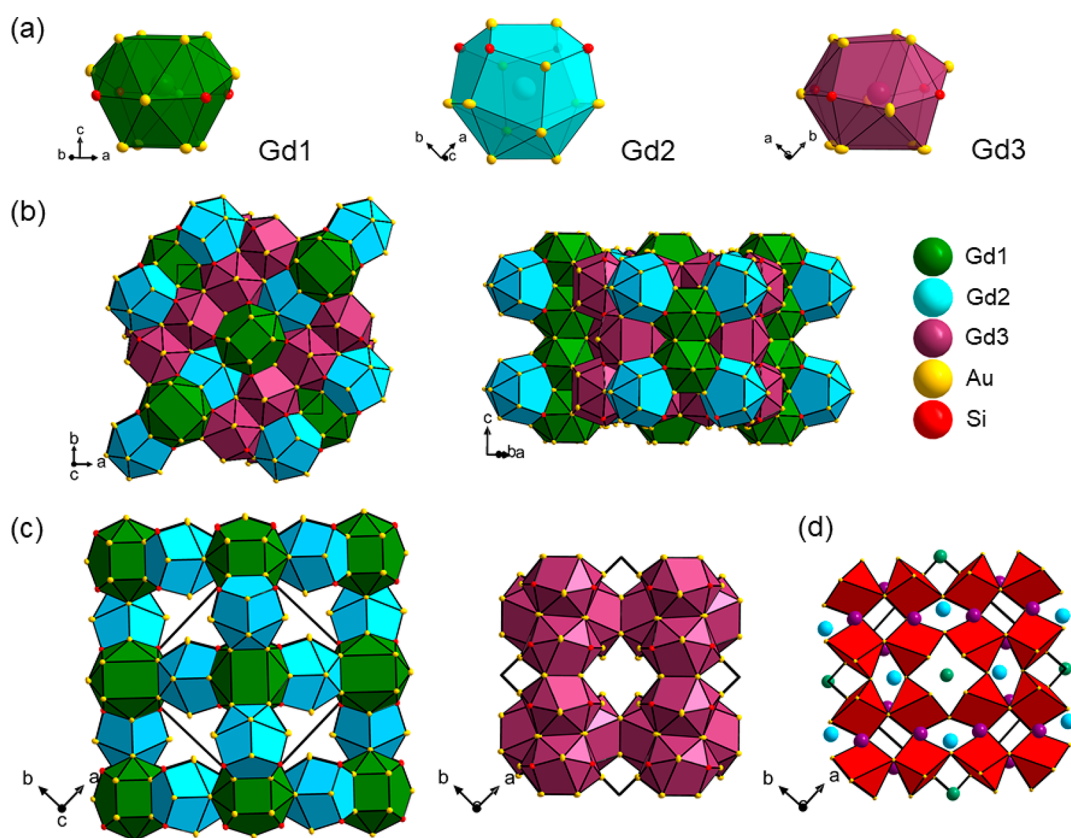
Figure 4. (a−c) Polyhedral crystal structure description for GdAu$_3$Si. Au and Si atoms are presented as thermal ellipsoids at the 70% probability level. (d) Polyanionic Au$_3$Si substructure corresponding to a framework of corner-connected Si-centered trigonal prims SiAu$_{6/2}$.
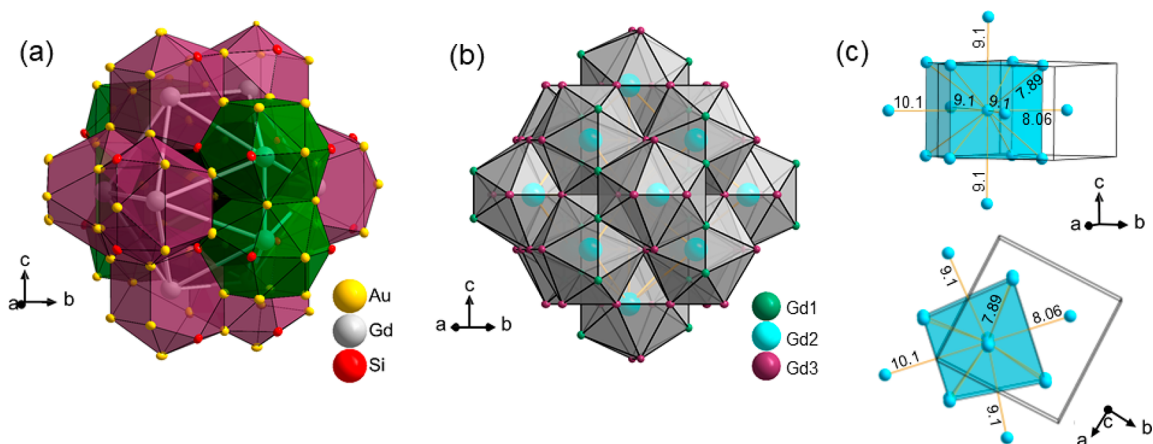
**Figure 5.** (a) Icosahedral environment of Gd2 by 4 Gd1 and 8 Gd3 atoms in the crystal structure of GdAu$_3$Si. (b and c) The bcc-like arrangement of Gd2(Gd1,Gd3)$_{12}$ icosahedra. (c) Only the icosahedra center (Gd2 atoms) are shown, and the Gd2−Gd2 distances are indicated.

AC(IT) and AC(CC) phases.[28] See the Supporting Information (and ref 42 therein) for more detailed information regarding electrical resistivity data (see Figures S6 and S7) and specific heat data analysis (see Figures S8 and S9).

3.4. Antiferromagnetic GdAu$_3$Si. The GdAu$_3$Si structure type provides a new type of magnetic sublattice forming a network of distorted icosahedron-like polyhedra (cf. Figure 5). We observe a Curie−Weiss behavior of the magnetic susceptibility M/H above ∼50 K with an effective magnetic moment of $p_{eff} = 7.99$ μ_B/Gd (see Figure S10), which is in good agreement with the theoretical value for a free Gd^{3+} ion (7.94 μ_B/Gd). The estimated Curie−Weiss temperature is θ_p

≈ −10 K, indicating that antiferromagnetic interactions are dominant. Figure 7a shows the temperature dependence of the magnetization (plotted as M/H) under the magnetic field of H = 5 and 50 kOe. We observe anomalies (denoted by T_A, T_B, and T_m^*) in the $M−T$ curve. Figure 7b shows the $M−H$ curves. We observe a slight meta-magnetic-like jump at $H_m^* \sim 10$ kOe and a linear behavior above $H_m^{**} \sim 50$ kOe, indicating possible changes in the configuration of magnetic order, yet the overall feature is of antiferromagnetic-type. See Figures S11−S15 for more detailed magnetization data. Figures 7c,d shows the temperature and magnetic field dependence of the electrical
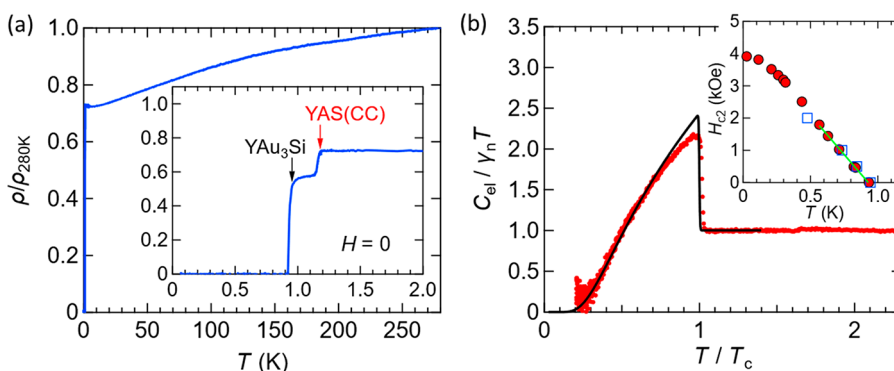
Figure 6. Superconductivity of YAu₃Si. (a) Temperature dependence of the normalized electrical resistivity (ρ/ρ_{280K}) under zero field; ρ_{280K} = 210 $\mu\Omega$ cm. The inset shows a close-up view for the resistivity near T_c. (b) Plot of $C_{el}/\gamma_n T$ as a function of T/T_c. We set T_c = 0.97 K, which is slightly larger than the value (T_c = 0.94 K) determined from the resistivity data. The solid curve indicates the theoretical curve expected from the weak-coupling BCS model. The inset shows the upper critical field H_{c2} as a function of temperature. The filled-symbol points are obtained from the resistivity data, while the open-symbol points are from the specific heat data.

Table 4. Superconducting Parameters of YAu₃Si[a].

parameter	YAu₃Si
T_c (K)	0.94
$H_{c2}(0)$ (kOe)	3.9
$H_c(0)$ (Oe)	69
$H_{c1}(0)$ (Oe)	4.5
κ	40
$\xi(0)$ (nm)	29
$\lambda(0)$ (μm)	1.2

[a]The lower critical field H_{c1} (T = 0) is estimated from the following relation $H_{c1} = H_c \ln(\kappa)/\sqrt{2}\kappa$, which is valid for large κ values.[41] The coherence length $\xi(T = 0)$ and penetration depth $\lambda(T = 0)$ are estimated from the following relations: $H_{c2}(0) = \Phi_0/2\pi\xi(0)^2$ and $\kappa \equiv \lambda/\xi$ where Φ_0 is the magnetic flux quanta.

resistivity, respectively. In the $\rho-H$ curve, we observe inflections at H_B and H_C for $T < 8$ K and steps at H_A.

Figure 8a depicts the temperature dependence of the specific heat (plotted as C/T) under various magnetic fields at low temperatures. We observe two notable peaks corresponding to T_A and T_B, suggesting two-step magnetic transitions. The peak at T_A is sharp for $H \leq 10$ kOe, becomes broad in the range of $15 \lesssim H \lesssim 40$ kOe, again becomes very sharp in $50 \lesssim H \lesssim 80$ kOe, and becomes broad above $H \gtrsim 90$ kOe (up to $H = 120$ kOe) with peak shifts toward lower temperatures as H increases. However, the peak at T_B shifts toward lower temperatures as H increases and turns into an inflection for $H \gtrsim 80$ kOe. The specific heat at $H = 90$ kOe exhibits an additional peak corresponding to T^*. The zero-field specific heat also exhibits a small anomaly at T^{**} and two inflections at T_B (denoted as T_B' = 4.94 K and T_B'' = 4.79 K) as shown in the insets of Figure 8a. Figure 8b depicts the magnetic field dependence of C/T at several temperatures around T_A. We observed anomalies corresponding to H_A, H_B, and H_C in the resistivity measurements. We estimated the magnetic contribution to the specific heat (C_{mag}) by estimating the lattice (phonon) contribution from the specific heat of YAu₃Si (Figure 8c) and calculated the magnetic entropy (ΔS_{mag}) above 0.2 K (Figure 8d). See the Supporting Information (and Figure S16 therein) for details. The magnetic entropy $\Delta S_{mag}(T)$ seems to saturate near $R \ln 8$ (where R is the gas constant) above the magnetic transition temperature T_A, indicating that Gd³⁺ ($J = 7/2$) magnetic moments become free

with almost full $(2J + 1)$-fold degeneracy (under crystal electric fields) above T_A, which is in line with typical Gd compounds.[43] Note that the deviation from the value of $R \ln 8$ may be attributed to the missing contribution from below the base temperature (0.2 K) and/or shortcomings in the estimated phonon contribution. Figure 9 shows the characteristic temperatures (T_A, T_B, T^*, T^{**}, and T_m^*) and magnetic fields (H_A, H_B, H_C, H_m^*, and H_m^{**}) obtained from the specific heat, magnetization, and electrical resistivity. It seems there are three different magnetic states below T_A, depending on the external magnetic field (as highlighted with green, red, and blue hatchings). Each state is further separated at T_B. We observe a hysteresis behavior crossing the H_A line for $70 \lesssim H \lesssim 90$ kOe, suggesting that the H_A line for $70 \lesssim H \lesssim 90$ kOe (probably terminated near a specific point denoted by T^*) is first-order-like.

To shed more light into the complex magnetic behavior of GdAu₃Si, MDMC simulations were carried out. For these simulations, four initial distributions of magnetic moments, namely, ferromagnetic (FM), paramagnetic (PM), and two types of the ferrimagnetic one, were considered (Figure 10). The paramagnetic distribution was created in a disordered local-moment (DLM) fashion[44] known to nicely mimic the true paramagnetic distribution while keeping magnetic moments collinear and the total magnetic moment equal to zero. The ferrimagnetic distribution of type 1 was created with magnetic moments at atoms on the Gd1 (4e) and Gd3 (8i) positions parallel to each other, while magnetic moments on the Gd2 (4f) position were aligned antiparallel to them. The ferrimagnetic distribution of type 2 was created with magnetic moments at atoms on the Gd2 and Gd3 positions in parallel, while the moments on the Gd1 position were antiparallel to them. Several initial distributions were tested in order to prove the convergence of all the starting configurations to the same magnetic state with the lowest energy. In addition, two values of the starting magnetic moment (3 and 7 μ_B per atom) were tested which resulted always in a high-spin state with magnetic moments of Gd equal to 7.08−7.1 μ_B. As already mentioned above, the resulting magnetic states were tested for a possible noncollinearity using the noncollinear version of VASP and appeared to be collinear.

As one can see from Figure 10, the initial FM distribution has the highest total energy, whereas the PM distribution has the lowest, which is rather close to the equilibrium magnetic
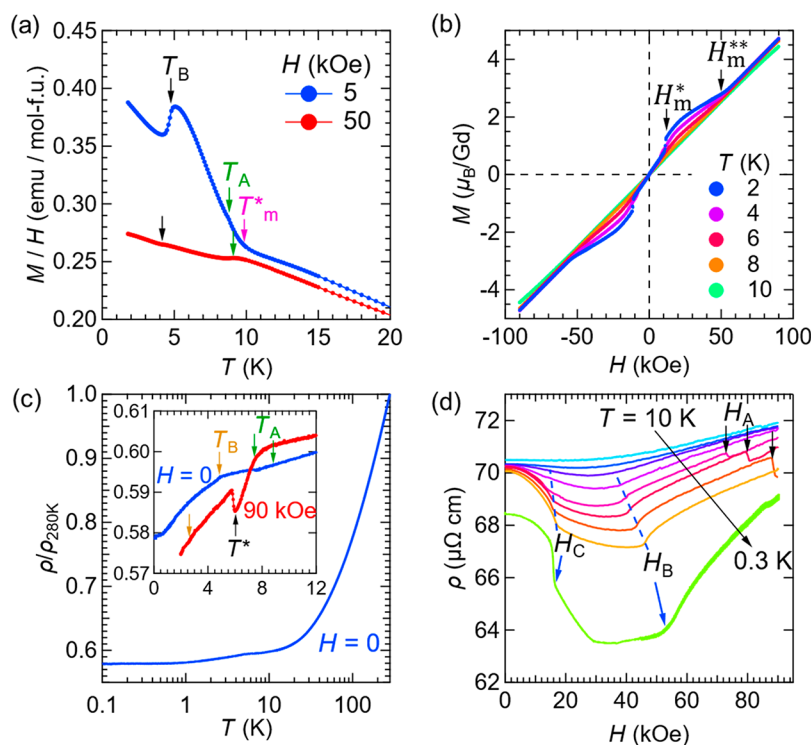
Figure 7. Magnetic and transport properties of GdAu$_3$Si. (a) Temperature dependence of magnetization (plotted as M/H) under $H = 5$ kOe and 50 kOe at low temperatures. (b) $M-H$ curves measured at several temperatures. The remarkable points, denoted by T_m^*, H_m^*, and H_m^{**}, are determined from the magnetization data. (c) Temperature dependence of the normalized electrical resistivity (ρ/ρ_{280K}) under zero field; $\rho_{280K} = 120\ \mu\Omega$ cm. The inset shows the close-up view of the low-temperature region including resistivity under the magnetic field of $H = 90$ kOe. (d) Magnetic-field dependence of electrical resistivity measured at $T = 0.3, 5.5, 6.3, 7.2, 7.7, 8.0, 8.5, 9.0,$ and 10 K. The specific temperatures (T_A, T_B, and T^*) and magnetic fields (H_A, H_B, and H_C) determined by the specific heat data are indicated by the arrows and broken lines. We note that "mol-f.u." in (a) refers to the formula unit GdAu$_3$Si.

state after the simulation. The energy differences between magnetic states are rather small. After approximately 160 MDMC steps, all considered initial distributions of magnetic moments converged to two configurations, which were very close in energy and remained unchanged through further MDMC runs. These two final states are antiferromagnetic (AFM), with 8 parallel and 8 antiparallel spins, and ferrimagnetic, with 9 parallel and 7 antiparallel spins (for the particular distributions, see Figure 11). Both states have collinear magnetism. As they are very close in energies (which should be considered as zero within the DFT accuracy), one might expect a frustrated magnetic behavior of the system. The collinear magnetic order suggests the presence of an easy-axis anisotropy.

4. DISCUSSION

The complex $T-H$ phase diagram shown in Figure 9, which includes several regions of $T-H$ in which the magnetic order is modulated, is reminiscent of centrosymmetric frustrated antiferromagnets (Gd-based intermetallic compounds) such as triangular lattice Gd$_2$PdSi$_3$[45] and breathing-kagome-lattice Gd$_3$Ru$_4$Al$_{12}$[46] whose intriguing chiral (topological) spin textures called skyrmion lattices were recently reported. Similar to these Gd-based frustrated antiferromagnets, GdAu$_3$Si has a centrosymmetric crystal structure (spatial inversion symmetry) with triangular magnetic units (which could cause geometrical frustration). Qualitatively one can assume the same exchange-coupling mechanism, i.e., Ruderman–Kittel–Kasuya–Yosida (RKKY)-type exchange interaction, which is also plausible

from the DOS of GdAu$_3$Si (cf. Figure S5b). However, GdAu$_3$Si has a three-dimensional crystal structure (rather than a (quasi) two-dimensional), and the triangular units constituting the icosahedra are distorted (cf. Figure 5b). The quasi-degenerate feature (energetically close-lying magnetic states) found in our simulation and the complex magnetic behavior for $H = 0$, which is represented by additional anomalies in the specific heat (i.e., the anomaly at T^{**} and the two-inflection behavior at T_B), may reflect magnetic frustration. The complex $T-H$ phase diagram of GdAu$_3$Si also bears some resemblance to those of noncentrosymmetric chiral-lattice magnets (with broken inversion symmetry) such as metallic MnSi[47] and insulating (multiferroic) Cu$_2$OSeO$_3$.[48] We note that the inversion symmetry with respect to magnetic Gd atoms is locally broken since the Gd2(Gd1,Gd3)$_{12}$ pseudo-icosahedron with the cluster-center Gd2 (see Figure 5b) does not have inversion symmetry, though the global inversion symmetry is conserved.

We also analyzed the critical behavior of the specific heat at the magnetic transition at T_A for $H = 0$, 5 and 60 kOe considering the minimal curve $C = A_\pm |t|^{-\alpha} + B + Lt$,[49] in which the first term describes a critical behavior, while the last two terms represent background contributions, where α, $A_\pm$, B, L are adjustable parameters and $t \equiv (T - T_N)/T_N$ (with $T_N \approx T_A$); see the Supporting Information (and Figure S17 therein) for details. α is a critical exponent, and the subscript "+" and "−" indicates $T > T_N$ and $T < T_N$, respectively. Our analysis suggests an approximate critical exponent of $\alpha = 0.2 \pm 0.04$ with $A_+/A_- \sim 0.66$ for $H = 0$ and 5 kOe (the green region in the $T-H$ diagram (see Figure 9), and $\alpha = 0.13 \pm 0.03$ with $A_+/$
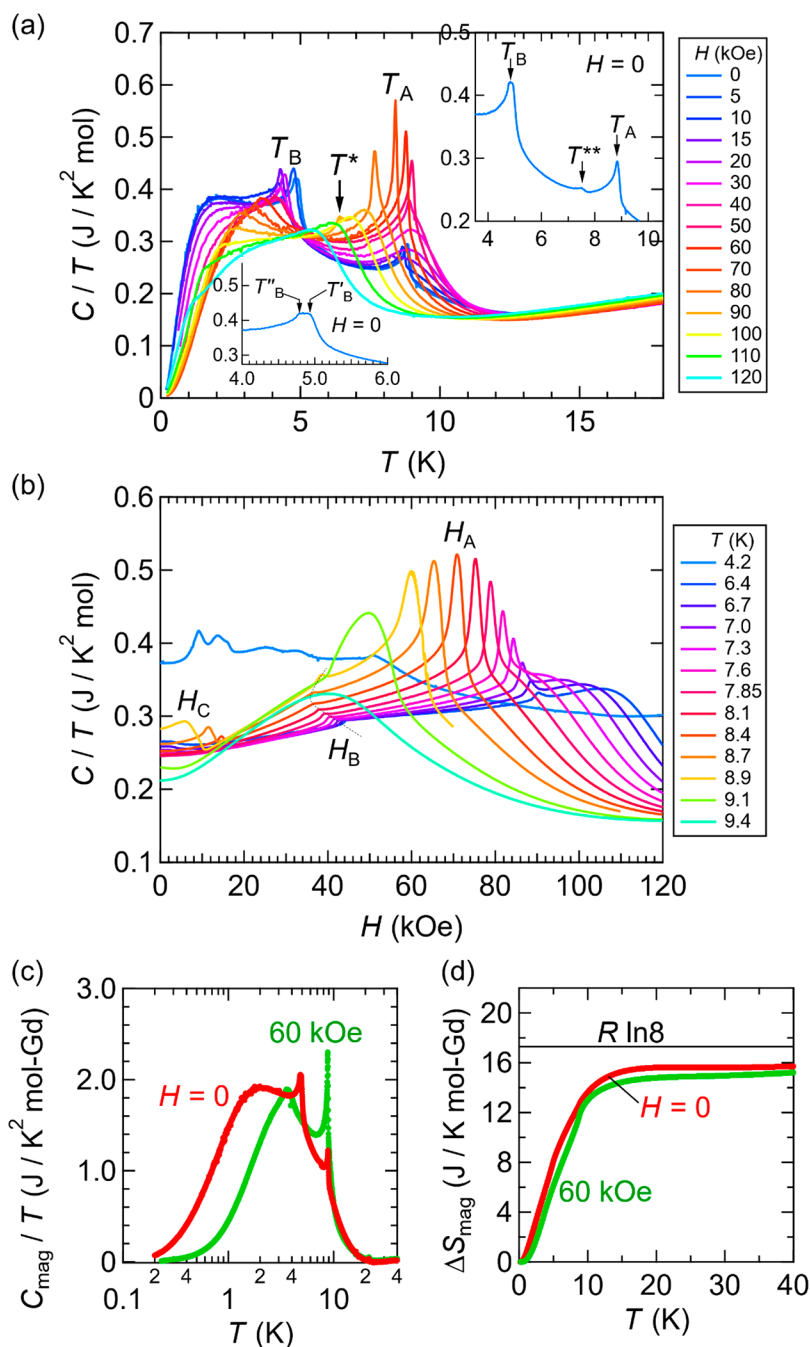
Figure 8. Specific heat of GdAu$_3$Si. (a) Temperature dependence of specific heat divided by temperature (C/T) for various values of magnetic fields. The upper-right inset shows a close-up view for a small anomaly denoted by T^{**}, while the lower-left inset shows a close-up view for the two inflections at T_B (denoted by T'_B and T''_B). Note that the two-inflection structure is absent for $H \geq 5$ kOe. (b) Magnetic field dependence of C/T. (c) Magnetic contribution to the specific heat (C_{mag}/T). (d) Magnetic entropy measured from $T \approx 0.2$ K (ΔS_{mag}). Note that the unit "mol" in (a) and (b) indicates the mole of Gd$_{0.2}$Au$_{0.6}$Si$_{0.2}$, while "mol-Gd" in (c) and (d) the mole of Gd atoms.

$A_- \sim 0.82$ for $H = 60$ kOe (the blue region). The latter α value is close to those of the universality class of 3D-Ising ($\alpha = 0.11$, $A_+/A_- = 0.52$).[49] This is in line with our computational result suggesting a uniaxial anisotropy. The low-field analysis ($H = 0$ and 5 kOe) yields parameters closer to those of the "chiral" Heisenberg type ($\alpha = 0.24 \pm 0.08$, $A_+/A_- = 0.54 \pm 0.2$).[50]

Interestingly, there is a qualitative similarity between the present GdAu$_3$Si system and the quasi-two-dimensional triangular Heisenberg frustrated antiferromagnets referred to as VX$_2$ (X = Cl, Br, and I), which have been studied with respect to the "chiral" universality class.[50,51] This similarity

between these completely different systems (having different structures and exchange-coupling mechanisms) may be due to the universality of the "chiral" Heisenberg class.[50] The VX$_2$ systems exhibit sharp peaks in their specific-heat curves at their magnetic transitions. According to refs 50 and 52, VCl$_2$ has a weak Ising-like anisotropy which causes two successive transitions in a very narrow temperature range, which is similar to the two-inflection structure at T_B observed in the specific heat ($H = 0$) of GdAu$_3$Si. We therefore conjecture that the uniaxial anisotropy (with the chiral Heisenberg behavior) plays an important role in GdAu$_3$Si. Also, VI$_2$ exhibits two
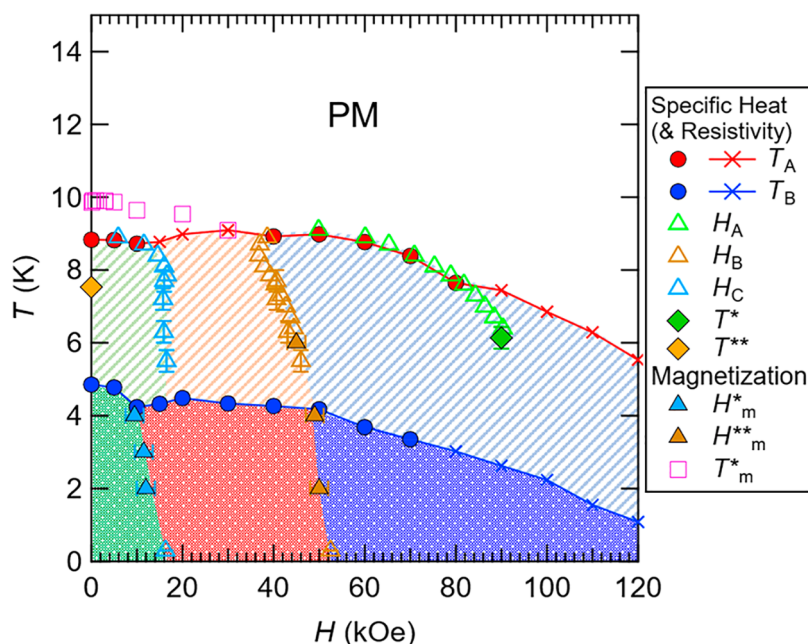
Figure 9. Characteristic data points (obtained from the specific heat, electrical resistivity and magnetization) plotted in the temperature vs magnetic field graph. For T_A and T_B, the cross symbols indicate that the anomalies are broad peaks or inflections, while the circle filled symbols are from the sharp peaks. The acronym PM indicates a paramagnetic phase.
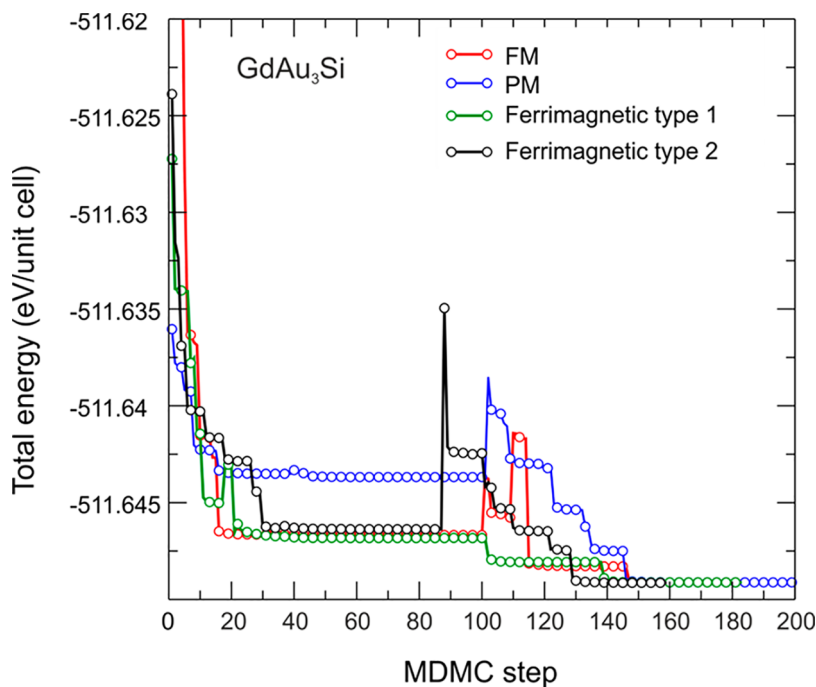

Figure 10. Relaxation of the total energy of GdAu$_3$Si with four initial distributions of magnetic moments: FM (shown with red line), PM (shown with blue line), and two ferrimagnetic (shown with green and black lines). Each third step of the MDMC simulation is shown with spheres of the corresponding colors.

distinct successive transitions (with respect to a transition to a 120° spin structure and to a collinear spin structure).[53] The latter exhibits a very sharp peak in its specific heat, which is similar to the very sharp peaks observed in the present system at T_A in $50 \lesssim H \lesssim 80$ kOe. From the similarity to VX$_2$ and the estimated critical exponents, it appears reasonable to suggest that GdAu$_3$Si has a chiral–Heisenberg nature (with a uniaxial anisotropy) in the low-field region (the green region, $H \lesssim 50$

kOe) and exhibits an Ising-like nature at the high-field region (the blue region, $H \lesssim 50$ kOe).

5. CONCLUSIONS

The investigation of reaction mixtures RE$_x$(Au$_{0.79}$Si$_{0.21}$)$_{100-x}$ (RE = Y and Gd) resulted in the compounds YAu$_3$Si and GdAu$_3$Si which crystallize in a new tetragonal structure type. The strictly (Au, Si) ordered structure features three crystallographically different RE atoms which are each
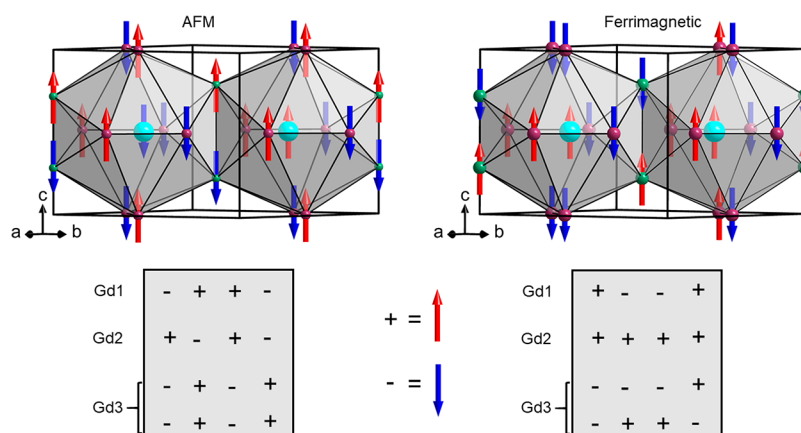
Figure 11. Distribution of magnetic moments in two neighboring icosahedral clusters $Gd2(Gd1,Gd3)_{12}$ for the two magnetic states corresponding to lowest total energies, as identified from MDMC simulations.

coordinated by 12 Au and 4 Si atoms. The $RE(Au,Si)_{16}$ polyhedra form interpenetrating frameworks in which the RE atom substructure corresponds to a bcc-like arrangement of centered icosahedra. Nonmagnetic YAu_3Si exhibits conventional BCS type-II superconductivity around 1 K. Antiferromagnetic $GdAu_3Si$ exhibits a multifarious $T-H$ phase diagram, which reflects its complex low temperature ($T \sim 10$ K) magnetic order. To characterize the $T-H$ phase diagram suggested in Figure 9, further investigations are required. Unfortunately, neutron-scattering experiments are hampered by the extraordinarily high absorption cross section of Gd. Similar to the compositionally neighboring cubic 1/1 AC phases ($RE(Au,Si)_{\sim 6}$), $REAu_3Si$ phases may be afforded for a larger range of RE which would give the opportunity for broader physical property studies associated with RE magnetism.

ASSOCIATED CONTENT

Supporting Information

The Supporting Information is available free of charge at https://pubs.acs.org/doi/10.1021/acs.inorgchem.1c03456.

> Plots of SEM/EDX, PXRD, DOS, and electron density iso-surface for YAu_3Si; list of interatomic distances for $REAu_3Si$ (RE = Gd and Y); plots of electrical resistivity and specific heat of YAu_3Si; plots of magnetization and specific heat of $GdAu_3Si$ (PDF)

Accession Codes

CCDC 2117650 and 2117652 contain the supplementary crystallographic data for this paper. These data can be obtained free of charge via www.ccdc.cam.ac.uk/data_request/cif, or by emailing data_request@ccdc.cam.ac.uk, or by contacting The Cambridge Crystallographic Data Centre, 12 Union Road, Cambridge CB2 1EZ, UK; fax: +44 1223 336033.

AUTHOR INFORMATION

Corresponding Authors

Girma Hailu Gebresenbut − *Department of Chemistry-Ångström Laboratory, Uppsala University, 751 21 Uppsala, Sweden;* orcid.org/0000-0003-1804-8259; Email: girma.gebresenbut@kemi.uu.se

Takayuki Shiino − *Department of Materials Science and Engineering, Uppsala University, 751 03 Uppsala, Sweden;* Email: takayuki.shiino@angstrom.uu.se

Authors

Lars Eriksson − *Department of Materials and Environmental Chemistry, Stockholm University, 106 91 Stockholm, Sweden*

Ulrich Häussermann − *Department of Materials and Environmental Chemistry, Stockholm University, 106 91 Stockholm, Sweden;* orcid.org/0000-0003-2001-4410

Andreas Rydh − *Department of Physics, Stockholm University, 106 91 Stockholm, Sweden*

Roland Mathieu − *Department of Materials Science and Engineering, Uppsala University, 751 03 Uppsala, Sweden;* orcid.org/0000-0002-5261-2047

Olga Yu. Vekilova − *Department of Materials and Environmental Chemistry, Stockholm University, 106 91 Stockholm, Sweden*

Complete contact information is available at: https://pubs.acs.org/10.1021/acs.inorgchem.1c03456

Author Contributions

The manuscript was written through contributions of all authors. All authors have given approval to the final version of the manuscript.

Notes

The authors declare no competing financial interest.

REFERENCES

(1) Smetana, V.; Rhodehouse, M.; Meyer, G.; Mudring, A.-V. Gold polar intermetallics: structural versatility through exclusive bonding motifs. *Accounts of chemical research* **2017**, *50* (11), 2633−2641.

(2) Smetana, V.; Lin, Q.; Pratt, D. K.; Kreyssig, A.; Ramazanoglu, M.; Corbett, J. D.; Goldman, A. I.; Miller, G. J. A Sodium-Containing Quasicrystal: Using Gold To Enhance Sodium's Covalency in Intermetallic Compounds. *Angewandte Chemie International Edition* **2012**, *51* (51), 12699−12702.

(3) Pham, J.; Meng, F.; Lynn, M. J.; Ma, T.; Kreyssig, A.; Kramer, M. J.; Goldman, A. I.; Miller, G. J. From quasicrystals to crystals with

interpenetrating icosahedra in Ca-Au-Al: in situ variable-temperature transformation. *J. Am. Chem. Soc.* **2018**, *140* (4), 1337−1347.

(4) Lin, Q.; Corbett, J. D. Approximant Phases and an Icosahedral Quasicrystal in the Ca- Au- Ga System: The Influence of Size of Gallium versus Indium. *Inorganic chemistry* **2008**, *47* (17), 7651−7659.

(5) Lin, Q.; Corbett, J. D. Development of the Ca-Au-In Icosahedral Quasicrystal and Two Crystalline Approximants: Practice via Pseudogap Electronic Tuning. *J. Am. Chem. Soc.* **2007**, *129* (21), 6789−6797.

(6) Ishimasa, T.; Tanaka, Y.; Kashimoto, S. Icosahedral quasicrystal and 1/1 cubic approximant in Au-Al-Yb alloys. *Philos. Mag.* **2011**, *91* (33), 4218−4229.

(7) Tanaka, K.; Tanaka, Y.; Ishimasa, T.; Nakayama, M.; Matsukawa, S.; Deguchi, K.; Sato, N. K. Tsai-type quasicrystal and its approximant in Au-Al-Tm alloys. *Acta Phys. Pol., A* **2014**, *126*, 603−607.

(8) Yamada, T.; Nakamura, Y.; Watanuki, T.; Machida, A.; Mizumaki, M.; Nitta, K.; Sato, A.; Matsushita, Y.; Tsai, A.-P. Formation of an Intermediate Valence Icosahedral Quasicrystal in the Au-Sn-Yb System. *Inorganic chemistry* **2019**, *58* (14), 9181−9186.

(9) Lin, Q.; Corbett, J. D. Development of an icosahedral quasicrystal and two approximants in the Ca-Au-Sn system: syntheses and structural analyses. *Inorganic chemistry* **2010**, *49* (22), 10436−10444.

(10) Ishikawa, A.; Hiroto, T.; Tokiwa, K.; Fujii, T.; Tamura, R. Composition-driven spin glass to ferromagnetic transition in the quasicrystal approximant Au-Al-Gd. *Phys. Rev. B* **2016**, *93* (2), 024416.

(11) Gebresenbut, G.; Tamura, R.; Eklöf, D.; Gómez, C. P. Syntheses optimization, structural and thermoelectric properties of 1/1 Tsai-type quasicrystal approximants in RE-Au-SM systems (RE = Yb, Gd and SM = Si, Ge). *Journal of Physics: Condensed Matter* **2013**, *25* (13), 135402.

(12) Tsai, A.-P.; Guo, J.; Abe, E.; Takakura, H.; Sato, T. A stable binary quasicrystal. *Nature* **2000**, *408* (6812), 537−538.

(13) Deguchi, K.; Matsukawa, S.; Sato, N. K.; Hattori, T.; Ishida, K.; Takakura, H.; Ishimasa, T. Quantum critical state in a magnetic quasicrystal. *Nature materials* **2012**, *11* (12), 1013−1016.

(14) Kamiya, K.; Takeuchi, T.; Kabeya, N.; Wada, N.; Ishimasa, T.; Ochiai, A.; Deguchi, K.; Imura, K.; Sato, N. Discovery of superconductivity in quasicrystal. *Nature communications* **2018**, *9* (1), 154.

(15) Takakura, H.; Gómez, C. P.; Yamamoto, A.; De Boissieu, M.; Tsai, A. p. Atomic structure of the binary icosahedral Yb-Cd quasicrystal. *Nat. Mater.* **2007**, *6* (1), 58−63.

(16) Goldman, A.; Kelton, R. Quasicrystals and crystalline approximants. *Rev. Mod. Phys.* **1993**, *65* (1), 213−230.

(17) Tsai, A. P. A test of Hume-Rothery rules for stable quasicrystals. *J. Non-Cryst. Solids* **2004**, *334*, 317−322.

(18) Gebresenbut, G.; Shiino, T.; Eklöf, D.; Joshi, D. C.; Denoel, F.; Mathieu, R.; Häussermann, U.; Pay Gómez, C. Atomic-Scale Tuning of Tsai-Type Clusters in RE-Au-Si Systems (RE= Gd, Tb, Ho). *Inorganic chemistry* **2020**, *59* (13), 9152−9162.

(19) Canfield, P.; Kong, T.; Kaluarachchi, U.; Jo, N. H. Use of frit-disc crucibles for routine and exploratory solution growth of single crystalline samples. *Philos. Mag.* **2016**, *96* (1), 84−92.

(20) Degen, T.; Sadki, M.; Bron, E.; König, U.; Nénert, G. The HighScore suite. *Powder Diffr.* **2014**, *29*, S13.

(21) Rodríguez-Carvajal, J. Recent advances in magnetic structure determination by neutron powder diffraction. *Physica B: Condensed Matter* **1993**, *192* (1−2), 55−69.

(22) *SAINT: APEX3 Software for CCD Diffractometers*; Bruker Analytical X-ray Systems Inc.: Madison, WI, 2014.

(23) Sheldrick, G. M. SHELXT - Integrated space-group and crystal-structure determination. *Acta Cryst.* **2015**, *A36* (1), 3−8.

(24) Petříček, V.; Dušek, M.; Palatinus, L. Crystallographic computing system JANA2006: general features. *Zeitschrift für Kristallographie-Crystalline Materials* **2014**, *229* (5), 345−352.

(25) Putz, H.; Brandenburg, K. *DIAMOND-Crystal and Molecular Structure Visualization*; Crystal Impact-GbR: Kreuzherrenstr, Germany, 2006.

(26) Momma, K.; Izumi, F. VESTA 3 for three-dimensional visualization of crystal, volumetric and morphology data. *J. Appl. Crystallogr.* **2011**, *44* (6), 1272−1276.

(27) Tagliati, S.; Krasnov, V. M.; Rydh, A. Differential membrane-based nanocalorimeter for high-resolution measurements of low-temperature specific heat. *Rev. Sci. Instrum.* **2012**, *83* (5), 055107.

(28) Shiino, T.; Gebresenbut, G. H.; Denoel, F.; Mathieu, R.; Häussermann, U.; Rydh, A. Superconductivity at 1 K in Y-Au-Si quasicrystal approximants. *Physical Review B* **2021**, *103* (5), 054510.

(29) Blöchl, P. E. Projector augmented-wave method. *Physical review B* **1994**, *50* (24), 17953.

(30) Kresse, G.; Furthmüller, J. Efficiency of ab-initio total energy calculations for metals and semiconductors using a plane-wave basis set. *Computational materials science* **1996**, *6* (1), 15−50.

(31) Kresse, G.; Furthmüller, J. Efficient iterative schemes for ab initio total-energy calculations using a plane-wave basis set. *Physical review B* **1996**, *54* (16), 11169.

(32) Kresse, G.; Joubert, D. From ultrasoft pseudopotentials to the projector augmented-wave method. *Physical review b* **1999**, *59* (3), 1758.

(33) Perdew, J. P.; Burke, K.; Ernzerhof, M. Generalized gradient approximation made simple. *Physical review letters* **1996**, *77* (18), 3865.

(34) Vekilova, O. Y. Efficient determination of the true magnetic structure in a high-throughput ab initio screening: the MDMC method. *arXiv (Materials Science)*, April 5, 2021, 2104.02106, ver. 1. https://arxiv.org/pdf/2104.02106

(35) Monkhorst, H. J.; Pack, J. D. Special points for Brillouin-zone integrations. *Physical review B* **1976**, *13* (12), 5188.

(36) Dudarev, S.; Botton, G.; Savrasov, S.; Humphreys, C.; Sutton, A. Electron-energy-loss spectra and the structural stability of nickel oxide: An LSDA+ U study. *Physical Review B* **1998**, *57* (3), 1505.

(37) Petersen, M.; Hafner, J.; Marsman, M. Structural, electronic and magnetic properties of Gd investigated by DFT+ U methods: bulk, clean and H-covered (0001) surfaces. *Journal of Physics: Condensed Matter* **2006**, *18* (30), 7021.

(38) Canfield, P. C. New materials physics. *Rep. Prog. Phys.* **2020**, *83* (1), 016501.

(39) Provino, A.; Steinberg, S.; Smetana, V.; Kulkarni, R.; Dhar, S. K.; Manfrinetti, P.; Mudring, A.-V. Gold-rich R 3 Au 7 Sn 3: establishing the interdependence between electronic features and physical properties. *Journal of Materials Chemistry C* **2015**, *3* (32), 8311−8321.

(40) Maple, M. B., Fischer, Ø., Eds. *Superconductivity in Ternary Compounds II: Superconductivity and Magnetism*; Topics in Current Physics Series, Vol. 34; Springer, 2013.

(41) Tinkham, M. *Introduction to Superconductivity*; Courier Corporation, 2004.

(42) Carbotte, J. Properties of boson-exchange superconductors. *Rev. Mod. Phys.* **1990**, *62* (4), 1027.

(43) Bouvier, M.; Lethuillier, P.; Schmitt, D. Specific heat in some gadolinium compounds. I. Experimental. *Physical Review B* **1991**, *43* (16), 13137.

(44) Gyorffy, B.; Pindor, A.; Staunton, J.; Stocks, G.; Winter, H. A first-principles theory of ferromagnetic phase transitions in metals. *Journal of Physics F: Metal Physics* **1985**, *15* (6), 1337.

(45) Kurumaji, T.; Nakajima, T.; Hirschberger, M.; Kikkawa, A.; Yamasaki, Y.; Sagayama, H.; Nakao, H.; Taguchi, Y.; Arima, T.-h.; Tokura, Y. Skyrmion lattice with a giant topological Hall effect in a frustrated triangular-lattice magnet. *Science* **2019**, *365* (6456), 914−918.

(46) Hirschberger, M.; Nakajima, T.; Gao, S.; Peng, L.; Kikkawa, A.; Kurumaji, T.; Kriener, M.; Yamasaki, Y.; Sagayama, H.; Nakao, H.; et al. Skyrmion phase and competing magnetic orders on a breathing kagomé lattice. *Nature Commun.* **2019**, *10* (1), 5831.

(47) Mühlbauer, S.; Binz, B.; Jonietz, F.; Pfleiderer, C.; Rosch, A.; Neubauer, A.; Georgii, R.; Böni, P. Skyrmion lattice in a chiral magnet. *Science* **2009**, *323* (5916), 915−919.

(48) Seki, S.; Yu, X.; Ishiwata, S.; Tokura, Y. Observation of skyrmions in a multiferroic material. *Science* **2012**, *336* (6078), 198−201.

(49) Oleaga, A.; Salazar, A.; Prabhakaran, D.; Cheng, J.-G.; Zhou, J.-S. Critical behavior of the paramagnetic to antiferromagnetic transition in orthorhombic and hexagonal phases of $RMnO_3$ (R = Sm, Tb, Dy, Ho, Er, Tm, Yb, Lu, Y). *Physical Review B* **2012**, *85* (18), 184425.

(50) Kawamura, H. Monte Carlo study of chiral criticality—XY and Heisenberg stacked-triangular antiferromagnets. *J. Phys. Soc. Jpn.* **1992**, *61* (4), 1299−1325.

(51) Takeda, K.; Uryû, N.; Ubukoshi, K.; Hirakawa, K. Critical exponents in the frustrated Heisenberg antiferromagnet with layered-triangular lattice: VBr_2. *J. Phys. Soc. Jpn.* **1986**, *55* (3), 727−730.

(52) Kadowaki, H.; Ubukoshi, K.; Hirakawa, K.; Martínez, J. L.; Shirane, G. Experimental study of new type phase transition in triangular lattice antiferromagnet VCl_2. *J. Phys. Soc. Jpn.* **1987**, *56* (11), 4027−4039.

(53) Kuindersma, S.; Haas, C.; Sanchez, J.; Al, R. Magnetic structures and properties of VI_2. *Solid State Commun.* **1979**, *30* (6), 403−408.